

# Trace Water-induced Morphology Engineering and Oxygen Vacancy for Enhancing the Capacity of $\text{Bi}_2\text{O}_3$ Alkaline Battery-Anode

Yanting Ma<sup>+</sup><sup>[a, b]</sup>, Yangyang Bai<sup>+</sup><sup>[a, b]</sup>, Yan Tang<sup>[a, b]</sup>, Shizheng Zheng,<sup>\*[a, b]</sup> Cuiqing Zhang,<sup>\*[c]</sup>, Changyuan Hu,<sup>\*[a, b]</sup> Kejie Dai<sup>[a, b]</sup>, Jing Zhao,<sup>[c]</sup> Qian Ding,<sup>[c]</sup> and Rongbin Zhang<sup>[d]</sup>

$\text{Bi}_2\text{O}_3$  is a theoretically high capacitive anode material; however, its low conductivity and deficient surface-active sites lead to reduced practical capability compared to the theoretical one. Herein, a facile and environmentally benign strategy is developed to simultaneously tailor the morphology and create oxygen vacancies in  $\text{Bi}_2\text{O}_3$  by adding trace water in a solvothermal procedure. Here trace water serves as an intermediary agent to change the growth mechanism of  $\text{Bi}_2\text{O}_3$  and form a hierarchical structure with increased crystallinity. Electrochemical experiments reveal that the optimal tremella-shaped  $\text{Bi}_2\text{O}_3$  delivers a higher specific capacity, approximately reaching

65% of the theoretical one. Such satisfactory electrochemical performance is due to the regulated tremella shape and the created oxygen vacancies, which can expose more electrochemical active-sites and promote ion diffusion. Moreover, the massive oxygen vacancies and increased crystallinity are also beneficial for electron transfer, thus enhancing the capacity. Eventually, a  $\text{Bi}_2\text{O}_3$ -6//AC asymmetric device is constructed and a superior energy density ( $40.8 \text{ Wh kg}^{-1}$ ) is realized than the others  $\text{Bi}_2\text{O}_3$ -based peers. This study paves a facile way for exploring advanced  $\text{Bi}_2\text{O}_3$ -based alkaline battery anode materials through an environmentally benign method.

## Introduction

Stimulated by the increasing global energy and environmental crisis, enormous efforts have been focused on exploiting environmental-benign energy storage devices, such as lithium-ion battery and alkaline rechargeable battery.<sup>[1]</sup> In particular, alkaline rechargeable batteries, which have a remarkable power density, fast charging, and ultra-long cycling lifespans, show a great potential as a future charge storage device.<sup>[2]</sup> However, unsatisfactory energy density is still the main drawback that hinders their large-scale application. Based on the formula  $E = 1/2 CV^2$ , the capacity of an electrode material is one of the key factors determining the energy density of alkaline rechargeable

battery devices.<sup>[3]</sup> Therefore, exploring advanced electrode materials with high capacities is a promising strategy for increasing energy density.

Recently, owing to its advantages of low cost and desirable environmental benignity,  $\text{Bi}_2\text{O}_3$  has attracted attention for energy storage and  $\text{CO}_2$  electrochemical reduction.<sup>[4]</sup> Moreover,  $\text{Bi}_2\text{O}_3$  possesses a high theoretical capacity ( $380 \text{ mAh g}^{-1}$ ), wide operating voltage window, and highly reversible redox process, making it a potential anode material.<sup>[5]</sup> Numerous studies have reported  $\text{Bi}_2\text{O}_3$  as a promising anode material, which displays a higher capacity than carbons, ascribed to the fast-faradic charge-storage mechanism on the surface.<sup>[6]</sup> In particular, solvothermal-synthesised  $\text{Bi}_2\text{O}_3$  with a sheet-like morphology can exhibit a high specific surface area, and thus, a modest capacity ( $329 \text{ F g}^{-1}$  at  $10 \text{ mVs}^{-1}$ ) is realised.<sup>[7]</sup> However, the actual capacity of  $\text{Bi}_2\text{O}_3$  is far from its theoretical value and does not meet the requirements of practical applications. The unsatisfactory actual capacity is mainly derived from the following aspects: 1) restacking of  $\text{Bi}_2\text{O}_3$  with less exposed electrochemical active sites, 2) poor conductivity with inferior electron transfer efficiency, and 3) architecture with deficient electrolyte permeation. Thus, overcoming the above-mentioned drawbacks and further increasing the capacity remain challenging.

Anchoring  $\text{Bi}_2\text{O}_3$  onto a conductive matrix, such as carbon fibres,<sup>[8]</sup> Ni/Ti form,<sup>[9]</sup> or graphene,<sup>[10]</sup> has been turn out to be an effective strategy for decorating  $\text{Bi}_2\text{O}_3$  by increasing the electron transfer efficiency. Nevertheless, no fundamental variation was observed in the intrinsic microstructure and conductivity of  $\text{Bi}_2\text{O}_3$ , and the improved capacity was limited; hence, more efforts should be made. Morphology modulation and oxygen vacancy creation are common strategies for

[a] Y. Ma,<sup>+</sup> Y. Bai,<sup>+</sup> Y. Tang, Prof. Dr. S. Zheng, Prof. Dr. C. Hu, K. Dai  
Jiangxi Key Laboratory of Surface Engineering  
Jiangxi Science and Technology Normal University  
No 589, Xuefu Road, Honggutan District, Nanchang 330013 (P.R. China)  
E-mail: zhengsz1990@163.com  
hcy6257@163.com

[b] Y. Ma,<sup>+</sup> Y. Bai,<sup>+</sup> Y. Tang, Prof. Dr. S. Zheng, Prof. Dr. C. Hu, K. Dai  
School of Materials and Mechanical & Electrical Engineering  
Jiangxi Science and Technology Normal University  
No 589, Xuefu Road, Honggutan District, Nanchang 330013 (P.R. China)

[c] C. Zhang, J. Zhao, Q. Ding  
School of Pharmacy  
Jiangxi Science and Technology Normal University  
No 605, Fenglin Road, Changbei, Nanchang 330038 (P.R. China)  
E-mail: cqzhang1992@163.com

[d] Prof. Dr. R. Zhang  
The Key Laboratory for Environment and Energy Catalysis of Jiangxi Province  
Nanchang University  
No 999, Xuefu Road, Honggutan District, Nanchang 330013 (P.R. China)

[+] These authors contributed equally to this work.

Supporting information for this article is available on the WWW under  
<https://doi.org/10.1002/batt.202300067>

tailoring  $\text{Bi}_2\text{O}_3$  to enhance its electrochemical performance by exposing more electroactive sites, promoting electrolyte permeation, and accelerating electron transfer.<sup>[11]</sup> Previous studies have demonstrated successful morphology regulation and electrochemical capacity improvement via the inclusion of surface-active agents in the solvothermal process.<sup>[11b,12]</sup> Additionally, owing to the narrowed bandgap and more exposed electrochemical active sites, creating oxygen vacancies through secondary chemical or thermal reduction also play a key role in increasing the capacity and stability of  $\text{Bi}_2\text{O}_3$ . Despite these achievements in morphology regulation and oxygen vacancy creation, there are still some problems that should be solved: 1) excess surface-active agents are difficult to completely remove and may lead to environmental pollution; and 2) high-temperature thermal reduction may cause structural damages. Therefore, exploring a novel and environment-friendly method to simultaneously realise morphology modulation and oxygen vacancy creation is highly desirable.

Therefore, in this study, a facile and environmentally benign path was designed to construct oxygen-vacancy-enriched  $\text{Bi}_2\text{O}_3$  with high electrochemical performance via the addition of trace water to the solvothermal system. Owing to the assembly of massive ultrathin nanosheets, tremella-shaped  $\text{Bi}_2\text{O}_3$  was fabricated, and the hierarchical structure guaranteed not only fast electrolyte permeation but electrochemically active sites exposure. The electrochemical results demonstrated that the optimal tremella-shaped  $\text{Bi}_2\text{O}_3$  delivered a high specific capacity of  $247 \text{ mAh g}^{-1}$  at  $1 \text{ A g}^{-1}$ , which is close to the theoretical value. Remarkable rate performance and long-term cycling stability were also realised because of the increased conductivity and crystallinity.

## Results and Discussion

### Structural characterization of water-tailored $\text{Bi}_2\text{O}_3$

A series of  $\text{Bi}_2\text{O}_3$  samples was synthesised via a facile solvothermal method using a varied ethanol-water mixture as the solvent (Figure 1a). As shown in Figure S1, when no or trace of water (less than 6 mL) was introduced into the beaker, the solution remained clear, and no sediment was observed. However, an apparent white precipitate appeared after superfluous water (12 or 24 mL) was decanted. Hence, introducing water into the solvothermal process has a significant impact on the growth mechanism of  $\text{Bi}_2\text{O}_3$ . Typically, without addition of water, Bi-glycol intermediate can slowly hydrolyze during the solvothermal process to form  $\text{Bi}_2\text{O}_3$  nanosheets. After introducing trace water into the reaction mixture, the hydrolysis rate was greatly accelerated and simultaneously forming large amounts of crystals with high surface free energy, which was then agglomerated into  $\text{Bi}_2\text{O}_3$  with a specific morphology.<sup>[13]</sup> However, when inclusion of massive water,  $\text{Bi}^{3+}$  was hydrolysed to  $\text{Bi(OH)}_3$  and then decomposed to  $\text{Bi}_2\text{O}_3$  during solvothermal process. To confirm the crystallinity and phase structure of the water-tailored  $\text{Bi}_2\text{O}_3$ , XRD was conducted (Figure 1b).  $\text{Bi}_2\text{O}_3$  synthesized with none of water displayed low crystallinity and

can be indexed to cubic  $\text{Bi}_2\text{O}_3$  according to the standard PDF card (JCPDS no. 27-0052) in the supplementary materials (Figure S2).<sup>[14]</sup> No phase transformation was appeared for  $\text{Bi}_2\text{O}_3$ -X ( $X = 3, 6, 12$ , and  $24$ ) after adding water in the solvothermal step, but the crystallinity was enhanced. Interestingly, with an increase in water volume, a gradually increased peak intensity was seen, and the highest intensity was achieved at a water volume of 24 mL. Therefore, adding water in the solvothermal step has a negligible effect on the phase type but can greatly improve the crystallinity. As reported previously, high crystallinity can decrease the structural defects or disorder and thus accelerate electron transfer, and thus is beneficial for improving the capacitive performance.<sup>[11d]</sup>

To identify the morphological and structural variation of  $\text{Bi}_2\text{O}_3$  after introducing water into the solvothermal process, SEM and TEM images were performed. As shown in Figure S3(a and b), thick  $\text{Bi}_2\text{O}_3$  sheets were formed using ethanol as the solo solvent, the thickness of which can be identified as dozens of nanometres. The corresponding TEM image in Figure S3(c) further verifies the thick sheet structure of  $\text{Bi}_2\text{O}_3$ , and the HRTEM (Figure S3d) shows the (220) plane with a lattice space of 0.19 nm. Nevertheless, after water was introduced into the solvothermal system, the morphology of  $\text{Bi}_2\text{O}_3$  changed greatly from thick sheets to ultrathin nanosheet-assembled hierarchical structure (Figure 1c and d). Specifically, when the water volume was 6 mL, tremella-shaped  $\text{Bi}_2\text{O}_3$  was composed of massive ultrathin nanosheets (Figure 1c). The further amplified SEM image in Figure 1(d) reveals that abundant caves were formed in tremella-shaped  $\text{Bi}_2\text{O}_3$  owing to the interconnected nanosheets, which will assist in exposing the electrochemical active sites and accelerating mass transfer.<sup>[6e]</sup> Additionally, the EDS mapping results in Figure 1(e) display the well-dispersed Bi, O, and C elements in the tremella-shaped structure, and the unexpected C element was likely derived from the residual ethylene glycol due to its high boiling point. According to the TEM image in Figure 1(f), the thickness of these nanosheets was approximately 5–10 nm, directly confirming the ultrathin structure of  $\text{Bi}_2\text{O}_3$ . The corresponding IFFT (Inverse Fast Fourier Transform) HRTEM image in Figure 1(g) reveals a lattice with an interplanar spacing of 0.32 nm, which is ascribed to the (111) facets. Such ultrathin nanosheet-assembled tremella structure can provide more electrochemically active sites and facilitate electrolyte permeation, which will undoubtedly enhance the capacity of  $\text{Bi}_2\text{O}_3$ .

To reveal the role of water in modulating the morphology and structure, SEM images of various water-tailored  $\text{Bi}_2\text{O}_3$  samples were obtained. As displayed in Figure 2(a–d), a strong correlation was found between the morphology and water addition volume. Typically, when trace water (3 mL) was introduced to the solvothermal process, an enormous morphology variation was observed (Figure 2a), and the thick sheets were converted to ultrathin nanosheets assembled hierarchical structure; however, the variation was not completed and some thick sheets could still be visualised. When the water volume was increased to 6 mL, nanosheet-assembled  $\text{Bi}_2\text{O}_3$  with a tremella shape was successfully formed owing to the accelerated hydrolysis process of Bi-glycol upon exposure to water

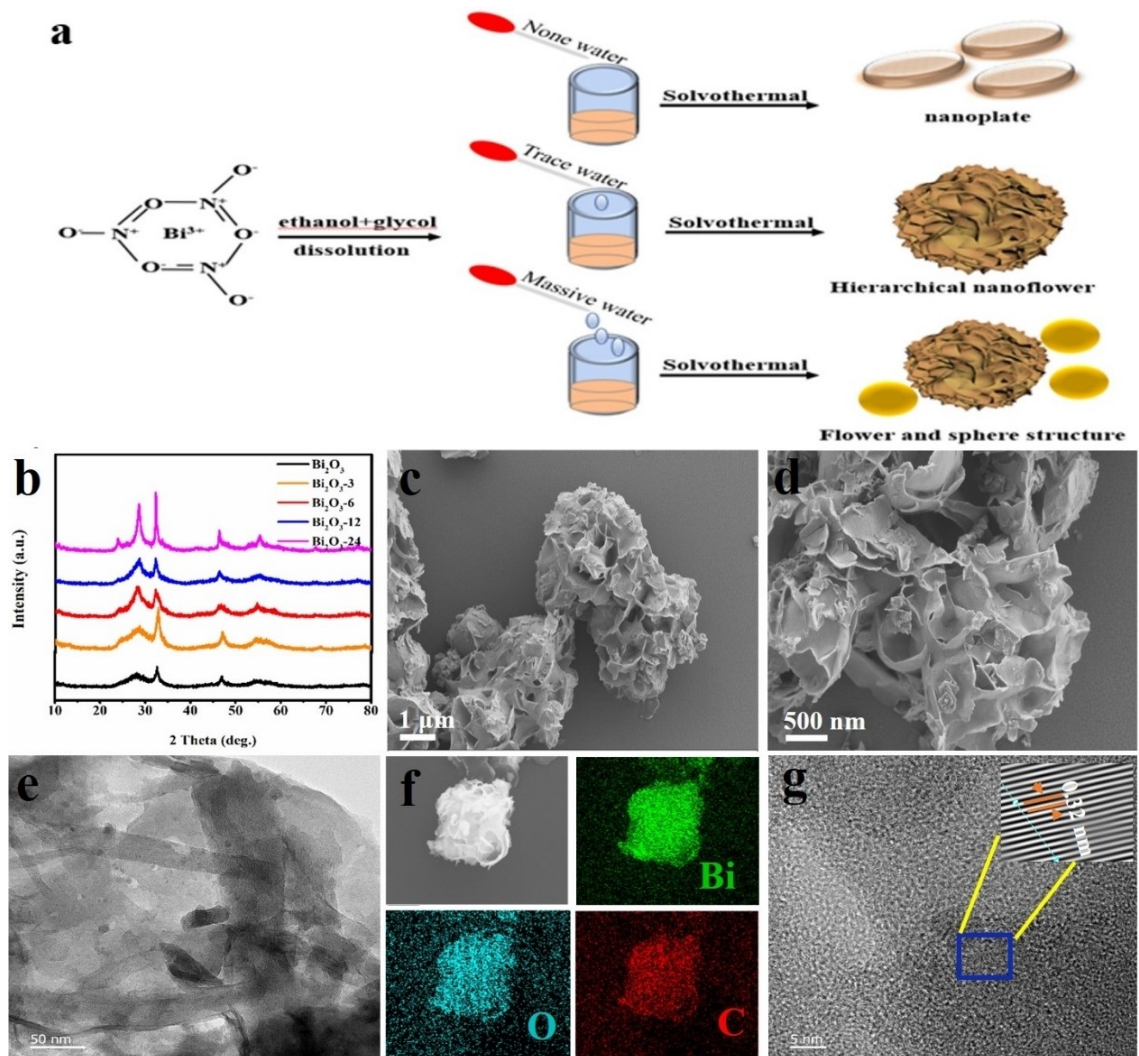


**Figure 1.** a) Illustration of the synthesis of a series of  $\text{Bi}_2\text{O}_3$  with various structures. b) XRD patterns of  $\text{Bi}_2\text{O}_3$  with various water addition. c and d) SEM images of  $\text{Bi}_2\text{O}_3\text{-}6$ . e) High-magnification TEM images of  $\text{Bi}_2\text{O}_3\text{-}6$ . f) TEM mapping analysis of Bi, O and C elements of the  $\text{Bi}_2\text{O}_3\text{-}6$ . g) HRTEM images of  $\text{Bi}_2\text{O}_3\text{-}6$ .

(Figure 2b). Nevertheless, with a further increase in the water volume to 12 mL, tremella-shaped  $\text{Bi}_2\text{O}_3$  was still visualised, but seriously stacked spheres began to appear (Figure 2c). The further amplified TEM image in Figure S4(a) directly demonstrates the formation of stacked spheres with diameter of 400–500 nm. The HRTEM image in Figure S4(b) shows an exposed (200) plane with a lattice space of 0.27 nm. Moreover, owing to the fast hydrolysis process, massive amounts of stacked  $\text{Bi}_2\text{O}_3$  spheres were obtained using absolute water as the solvent (Figure 2d). The stacked sphere-shaped  $\text{Bi}_2\text{O}_3$  is harmful for the exposure of electrochemical active sites and the permeation of electrolyte ions, and thus inhibiting the improvement of the capacity. Based on the above considerations, adding appropriate water in the solvothermal process would accelerate the hydrolysis of Bi-glycol and thus produce tremella-shaped  $\text{Bi}_2\text{O}_3$  with more electrochemical active sites exposed, which is favourable for increasing the capacitive behaviour.

$\text{N}_2$  absorption-desorption was then performed to ensure the specific surface areas and porous structure of series  $\text{Bi}_2\text{O}_3$

sample. As displayed in Figure 3(a), obvious hysteresis loops were observed in the  $P/P_0$  ranging from 0.6 to 1.0, indicative of the H3 type with a porous structure.<sup>[12a]</sup> According to the  $\text{N}_2$  absorption-desorption curves, the BET specific surface areas were calculated as 33, 26, 30, 26 and 23  $\text{m}^2 \text{g}^{-1}$  for  $\text{Bi}_2\text{O}_3$ ,  $\text{Bi}_2\text{O}_3\text{-}3$ ,  $\text{Bi}_2\text{O}_3\text{-}6$ ,  $\text{Bi}_2\text{O}_3\text{-}12$  and  $\text{Bi}_2\text{O}_3\text{-}24$ , respectively. Ascribing to the ultrathin  $\text{Bi}_2\text{O}_3$  nanosheet-assembled architecture,  $\text{Bi}_2\text{O}_3\text{-}6$  displayed higher specific surface area than others water-tailored  $\text{Bi}_2\text{O}_3$ , but smaller than that of  $\text{Bi}_2\text{O}_3$ . Generally speaking, the enhanced surface areas and porous structures can provide more electrochemically active sites and contribute to the ion diffusion process,<sup>[15]</sup> resulting in the remarkable capacity and rate ability. However, the specific surface area is not the only factor that determine the capacitive performance, which can also be affected by the conductivity and oxygen vacancy concentration of  $\text{Bi}_2\text{O}_3$ .

The composition and chemical status of series  $\text{Bi}_2\text{O}_3$  samples were further characterized via XPS, and the results were displayed in Figures 3(b and c) and S3. The survey spectra

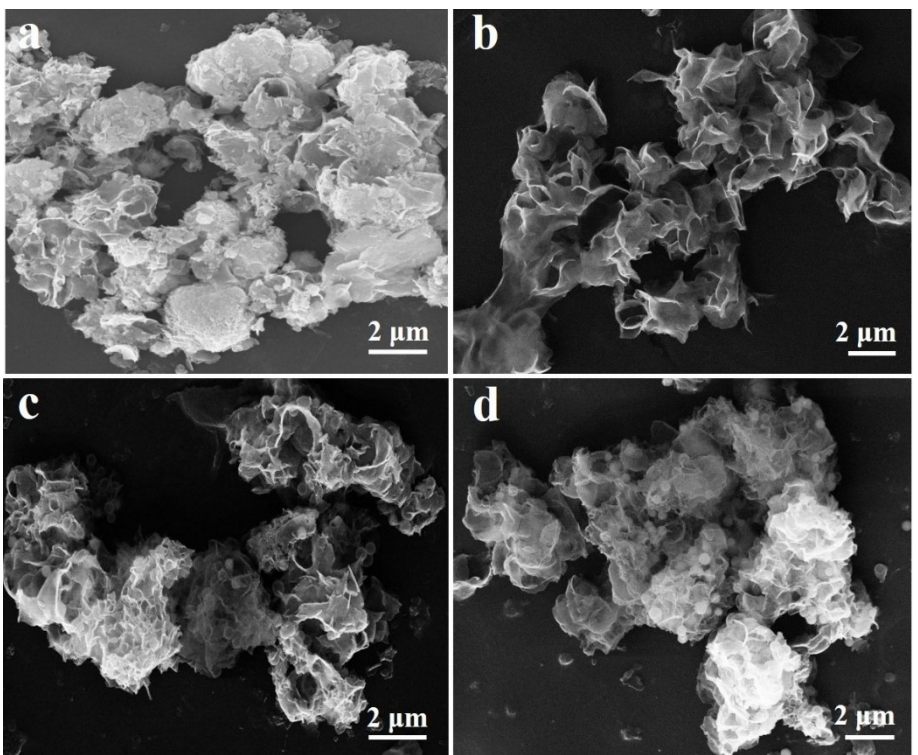


**Figure 2.** SEM images of various water tailored  $\text{Bi}_2\text{O}_3$ , a)  $\text{Bi}_2\text{O}_3$ -3, b) $\text{Bi}_2\text{O}_3$ -6, c)  $\text{Bi}_2\text{O}_3$ -12, and d)  $\text{Bi}_2\text{O}_3$ -24.

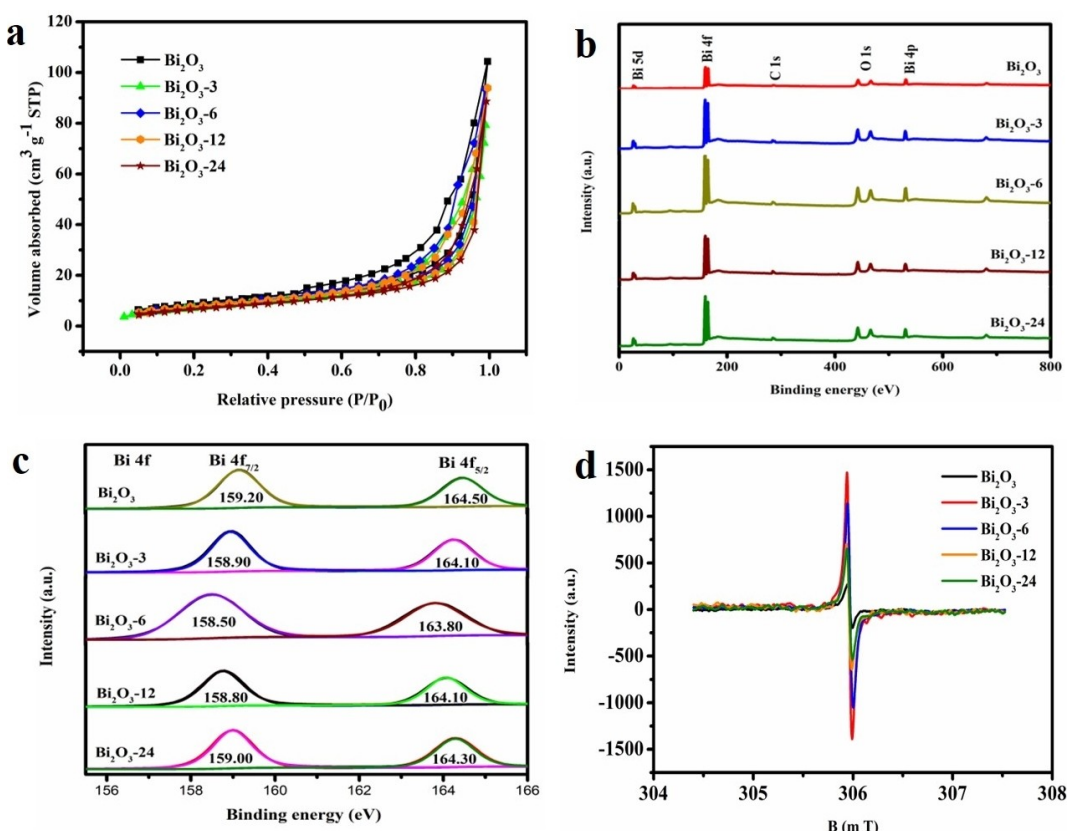
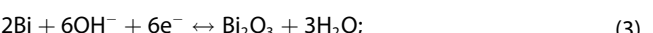


**Figure 3.** a)  $\text{N}_2$  adsorption-desorption isotherms of  $\text{Bi}_2\text{O}_3$  and  $\text{Bi}_2\text{O}_3$ -x. The XPS b) full spectrum of the survey, c)  $\text{Bi} 4f$  and d) EPR spectra of  $\text{Bi}_2\text{O}_3$  and  $\text{Bi}_2\text{O}_3$ -x, respectively.

demonstrated elemental Bi, O, and C in these samples, and no other impure elements were detected (Figure 3b). The Bi 4f high-resource spectrum of series  $\text{Bi}_2\text{O}_3$  can be divided into two peaks (Figure 3c), indexed to the  $4f_{7/2}$  (158.5 eV) and  $4f_{5/2}$  (163.8 eV) atom orbits, respectively. Interestingly, an obvious negative shift of the binding energy is displayed in comparison to pristine  $\text{Bi}_2\text{O}_3$ , confirming the higher electron density on the surface of water-tailored  $\text{Bi}_2\text{O}_3$ .<sup>[4b]</sup> Specifically, maximum negative shift was realised for  $\text{Bi}_2\text{O}_3$ -6, and such higher electron density indicative of the highest oxygen vacancy concentration on the surface of  $\text{Bi}_2\text{O}_3$ -6.<sup>[16]</sup> Additionally, the Bi–O lattice peak in the O 2s spectrum of  $\text{Bi}_2\text{O}_3$ -6 also showed the similar negative shift, further confirming the higher electron density and the formation of oxygen vacancy (Figure S5). To directly prove the existence of oxygen vacancies, EPR spectra of  $\text{Bi}_2\text{O}_3$  and water tailored  $\text{Bi}_2\text{O}_3$ -x were then performed and compared in Figure 3(d). Obviously, compared to  $\text{Bi}_2\text{O}_3$ , a much stronger EPR signal is displayed at approximately  $g=1.99$  for water-tailored  $\text{Bi}_2\text{O}_3$ , and highest EPR signal was delivered in the  $\text{Bi}_2\text{O}_3$ -3, verifying the densest paramagnetic centres.<sup>[17]</sup> These oxygen vacancies serve as not only shallow donors to increase the carrier concentration but create more electrochemically active sites,<sup>[18]</sup> and thus enhancing the capacity.

### Electrochemical evaluation of $\text{Bi}_2\text{O}_3$

To reveal the effect of water addition on the capacity of  $\text{Bi}_2\text{O}_3$ , the electrochemical behaviours of the series  $\text{Bi}_2\text{O}_3$  was evaluated in 1 M KOH. As shown in Figure 4(a), typical battery behavior is observed with obvious redox peaks located at  $-0.8$  V,  $-0.6$  V and  $-0.4$  V, which represent the occurrence of the following reactions [Equations (1)–(3)].<sup>[9a,12a]</sup>



Water-tailored  $\text{Bi}_2\text{O}_{3-x}$  covers a larger integral area in the CV curves, demonstrating its enhanced capacitive ability, compared to that of common  $\text{Bi}_2\text{O}_3$ . Furthermore, as the water volume increased, the capacity gradually increased, and the optimal capacity was realised at a water volume of 6 mL. Further increasing the water volume (12 mL and 24 mL) could lead to a continuous shrinking of the CV profile, representing a gradually decreasing capacity. This phenomenon can be explained by the SEM results, which show that adding excess water would result in the formation of spheres and thus reduce the number of exposed electrochemical active sites (Figure 2c and d). Additionally, for the water-tailored  $\text{Bi}_2\text{O}_3$ , the anode and cathode peaks shifted to opposite directions, leading to a narrow potential gap between them. This unique phenomenon is probably due to the increased reversibility of surface redox reactions and enhanced conductivity.

The battery performance of series  $\text{Bi}_2\text{O}_3$  was directly evaluated via GCD curve. As shown in Figure 4(b), a typical battery-like merit is also identified for series  $\text{Bi}_2\text{O}_3$  due to the obvious charge and discharge plateaus at a potential of approximately  $-0.4$  V to  $-0.6$  V, the potential location of which agrees well with the redox peaks in the CV curves. As expected, all the water-tailored  $\text{Bi}_2\text{O}_3$  electrodes displayed longer discharge times at of  $1\text{ A g}^{-1}$ , revealing enhanced capacity, compared to pristine  $\text{Bi}_2\text{O}_3$ . Moreover, highest capacity was realized for the tremella-shaped  $\text{Bi}_2\text{O}_3$ -6, which was consistent with the CV results. A reasonable rule is also seen in the GCD results as CVs: capacity decreased with a further increase in

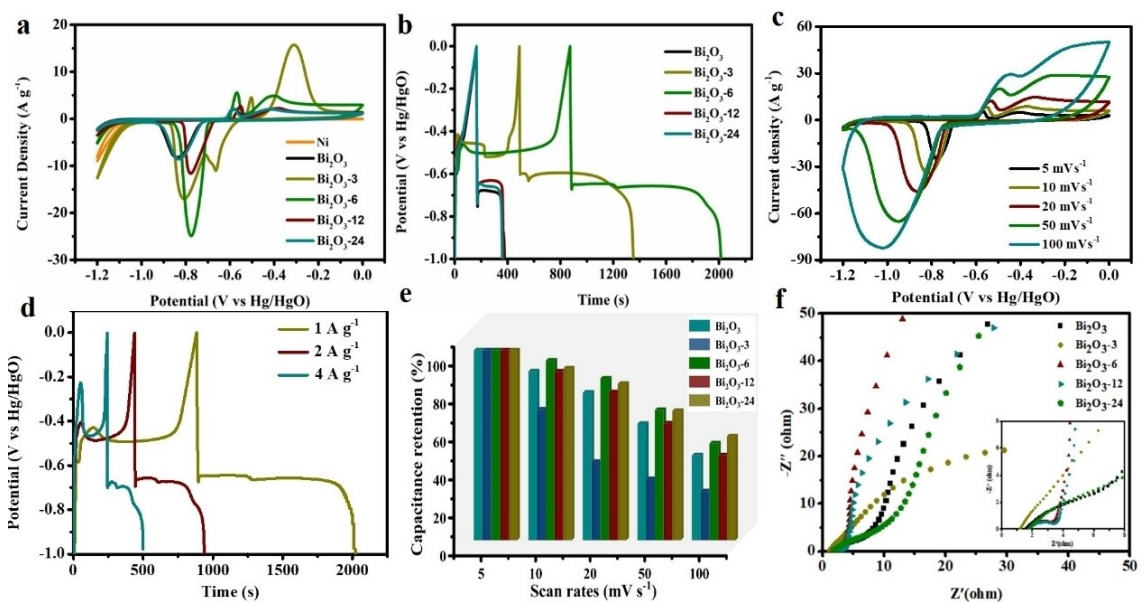


**Figure 4.** a and b) CV and GCD curves of series  $\text{Bi}_2\text{O}_3$  at  $5\text{ mVs}^{-1}$  and  $1\text{ A g}^{-1}$  respectively, c and d) CV and GCD curves of  $\text{Bi}_2\text{O}_3$ -6 at various scan rates and current densities, e) the capacity retention of series  $\text{Bi}_2\text{O}_3$  at various scan rates (from  $5\text{ mVs}^{-1}$  to  $100\text{ mVs}^{-1}$ ), f) EIS curves of series  $\text{Bi}_2\text{O}_3$ .

water volume. According to Equation (8) (Experimental Section), the specific capacity at  $1 \text{ Ag}^{-1}$  were calculated to be  $48 \text{ mAh g}^{-1}$  ( $48 \text{ mAh cm}^{-2}$ ),  $138 \text{ mAh g}^{-1}$  ( $138 \text{ mAh cm}^{-2}$ ),  $247 \text{ mAh g}^{-1}$  ( $247 \text{ mAh cm}^{-2}$ ),  $49 \text{ mAh g}^{-1}$  ( $49 \text{ mAh cm}^{-2}$ ) and  $48 \text{ mAh g}^{-1}$  ( $48 \text{ mAh cm}^{-2}$ ) for  $\text{Bi}_2\text{O}_3$ ,  $\text{Bi}_2\text{O}_3\text{-}3$ ,  $\text{Bi}_2\text{O}_3\text{-}6$ ,  $\text{Bi}_2\text{O}_3\text{-}12$  and  $\text{Bi}_2\text{O}_3\text{-}24$ , respectively. Compared to the previously reported  $\text{Bi}_2\text{O}_3$ , the water-tailored tremella-shaped  $\text{Bi}_2\text{O}_3\text{-}6$  achieves a superior specific capacity (Table S1, Supporting Information).

To acquire the refined capacitive performance of the optimal tremella-shaped  $\text{Bi}_2\text{O}_3\text{-}6$ , various CV and GCD curves were measured and are shown in Figure 4(c and d). Evidently, no significant CV profile change was observed, verifying the remarkable capacitive and rate performances. Additionally, the CV curves of the other  $\text{Bi}_2\text{O}_3$  samples are provided in Figure S6(a-d), and they both exhibit CV merits similar to those of  $\text{Bi}_2\text{O}_3\text{-}6$ . Moreover, all the  $\text{Bi}_2\text{O}_3$  samples show charge and discharge plateaus at potentials of approximately  $-0.4 \text{ V}$  and  $-0.6 \text{ V}$  in GCD curves (Figures 4d and S7a-d), and these results agree well with the redox peaks in the CV results. Additionally, the capacity retention of the series  $\text{Bi}_2\text{O}_3$  was calculated, and the results are displayed in Figure 4(e). Apparently, with an increase in current density, the specific capacity decreased gradually; but the trace-water tailored  $\text{Bi}_2\text{O}_3\text{-}x$  ( $x=3$  or 6) exhibited a higher capacity retention than the counterparts. Hence, adding an appropriate amount of water increases the capacitive and ratio performances of  $\text{Bi}_2\text{O}_3$  by tailoring the morphology, crystallinity, and surface oxygen vacancies.

To reveal the derivation of the superior electrochemical behaviours of water-tailored  $\text{Bi}_2\text{O}_3$ , EIS and MS plots were obtained, as shown in Figures 4(f) and S8. It is well-known that the EIS plot is important strategy that can reflect the electron-transfer and ion-diffusion status of the electrode.<sup>[3b,19]</sup> Typically, a larger linear slope is displayed for tremella-shaped  $\text{Bi}_2\text{O}_3\text{-}6$  in the low-frequency region, confirming a relatively faster ion-diffusion rate (Figure 4f). Additionally, the smallest diameter of the semicircle ( $2 \Omega$ ) is exhibited for tremella-shaped  $\text{Bi}_2\text{O}_3\text{-}6$ , compared to the other  $\text{Bi}_2\text{O}_3$  samples, demonstrating a lower electron-transfer resistance (inset of Figure 4f). The charge carrier densities were quantified using MS plots according to the following Equation (4):<sup>[14]</sup>

$$N = (2/e\epsilon_0\epsilon)[d(1/C^2)/dV]^{-1} \quad (4)$$

where,  $N$  is the charge carrier density (acceptor for p-type and donor for n-type),  $e$  is the electron charge,  $\epsilon$  is the dielectric constant of  $\text{Bi}_2\text{O}_3$ ,  $\epsilon_0$  is the permittivity of vacuum,  $C$  is the space charge capacitance in  $\text{F cm}^{-2}$ , and  $V$  is the potential applied at the electrode.<sup>[20]</sup> In the MS plots, both  $\text{Bi}_2\text{O}_3$  and  $\text{Bi}_2\text{O}_3\text{-}6$  exhibit n-type semiconductor behaviour with positive slopes of  $2.106 \times 10^6$  and  $1.558 \times 10^6$ , respectively. According to the calculation, the  $\text{Bi}_2\text{O}_3\text{-}6$  electrode realizes a higher donor density ( $4.98 \times 10^{22} \text{ cm}^{-3}$ ) than  $\text{Bi}_2\text{O}_3$  ( $3.68 \times 10^{22} \text{ cm}^{-3}$ ), directly indicating the higher electron conductivity of  $\text{Bi}_2\text{O}_3\text{-}6$ . Based on the above results, a lower electron-transfer resistance and faster mass transfer are the two advantages that contribute to superior electrochemical behaviour. This can be explained by more oxygen vacancies, and the ultrathin nanosheets as-

sembled a tremella morphology with a high specific surface area and shortened diffusion paths.

To identify the charge-storage mechanism of trace water-tailored  $\text{Bi}_2\text{O}_3$ , the current contributions from surface-controlled processes and diffusion-controlled behaviour were analyzed using the following Equation (5):<sup>[21]</sup>

$$I(V) = av^b \quad (5)$$

where,  $a$  and  $b$  are the appropriate values. Commonly, a value of  $b$  close to 0.5 implies that the current is mainly derived from the surface-controlled process, while a value of  $b$  close to one reveal diffusion-controlled behaviour to the total current. Accordingly,  $b$  value of 0.64 and 0.59 is respectively obtained based on the anode and cathode peak currents (Figure 5a), verifying that the surface-controlled and diffusion-controlled process both contributed to the capacity. Moreover, to precisely quantify each contribution, a new equation [Equation (6)] was derived as follows:<sup>[1c]</sup>

$$i(V) = k_1v + k_2v^{1/2} \quad (6)$$

where,  $k_1$  and  $k_2$  can be obtained from the slope and intercept of the straight-line Equation (7) as follows:

$$i(V)/v^{1/2} = k_1v^{1/2} + k_2 \quad (7)$$

The surface capacitive contribution was verified according to the above equation, and the obtained voltage profile is shown in Figure 5(b). Based on the calculation, a surface capacitive contribution of 40% was delivered at  $1 \text{ mVs}^{-1}$  and with an increase in the scan rate, an improved surface capacitive contribution was realized (Figure 5c), confirming highly efficient surface charge storage. Such performance probably stemmed from the oxygen vacancy and high crystalline structure with more exposed active sites and increased conductivity.

As long-term stability is one of the significant augments to assess electrode materials, continuous CV cycling was executed for tremella-shaped  $\text{Bi}_2\text{O}_3\text{-}6$ . With the increase of CV cycling, the capacity of  $\text{Bi}_2\text{O}_3\text{-}6$  shows a gradual attenuation, and when the cycling number reaches 1500, approximately 82% of the initial capacity is retained (Figure 5d). As previously reported, the unsatisfactory stability originates from the dissolution of  $\text{Bi}_2\text{O}_3$  in the continuous charge and discharge process;<sup>[11d]</sup> thus, improving the stability of  $\text{Bi}_2\text{O}_3$  is imperative in a subsequent study.

Based on the above results, the addition of trace water cannot only tailor the morphology and enhance the crystallinity but also create massive oxygen vacancies on the surface of  $\text{Bi}_2\text{O}_3$ . The superior electrochemical behaviour of tremella-shaped  $\text{Bi}_2\text{O}_3$  originates from the synergistic effect of the following aspects: i) the enhanced crystallinity and created oxygen vacancies to improve the conductivity and electron transfer efficiency; ii) the ultrathin nanosheets assembled with the tremella morphology to expose more electrochemically

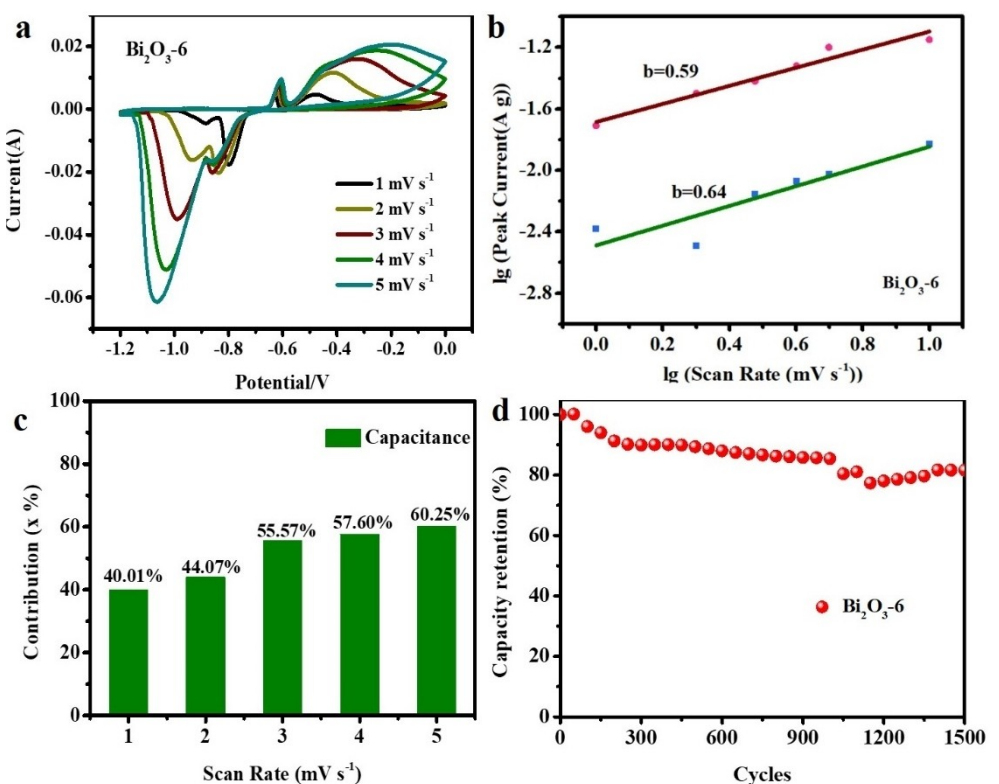


**Figure 5.** a) CV curves of  $\text{Bi}_2\text{O}_3\text{-}6$  at various scan rates, b) relationship between  $\log(i)$  and  $\log(v)$  plots of the anodic and cathodic peak currents at scan rates of  $1 \text{ mV s}^{-1}$  to  $10 \text{ mV s}^{-1}$ . c) Histogram of the capacitive contribution at various scan rates of  $\text{Bi}_2\text{O}_3\text{-}6$ . d) Stability performance of  $\text{Bi}_2\text{O}_3\text{-}6$  evaluated via 1500 continuous CV cycling with scan rate of  $100 \text{ mV s}^{-1}$ .

active sites; and iii) a tremella-shaped hierarchical structure to promote ion transfer and shorten the diffusion paths.

#### Assembly of asymmetric device and charge storage performance evaluation

To explore the possibility of actual applications, asymmetric device was constructed using  $\text{Bi}_2\text{O}_3$  or  $\text{Bi}_2\text{O}_3\text{-}6$  as the anode and AC as the cathode (Figure 6a), and the charge storage performance was evaluated. At first, the work potential window of  $\text{Bi}_2\text{O}_3\text{-}6//\text{AC}$  asymmetric device was measured and can reach  $1.6 \text{ V}$  (Figure 6b), which guarantees remarkable energy density. Moreover, a pair of redox peaks was seen, confirming the battery-like charge-storage mechanism. With an increase in the scan rate, the CV profiles showed no significant change, revealing remarkable charge-storage performance and ratio performance. Further GCD measurements were then performed to directly verify the charge/discharge capability and the apparent plateau attributed to Faraday redox reactions (Figure 6c). According to Equation (8), the capacity of the  $\text{Bi}_2\text{O}_3\text{-}6//\text{AC}$  asymmetric device can be calculated to be  $51$ ,  $22.5$ ,  $9.2$ , and  $3.6 \text{ mAh g}^{-1}$  at  $1$ ,  $2$ ,  $4$ , and  $8 \text{ A g}^{-1}$ . Clearly, as the current density increased, the capacity of the device gradually decreased, revealing a remarkable ratio performance. As a comparison, the capacitive performance of  $\text{Bi}_2\text{O}_3//\text{AC}$  asymmetric device was also evaluated (Figure S9a and b) and contrasted in Figure 6(d

and e). The capacitance of  $\text{Bi}_2\text{O}_3//\text{AC}$  asymmetric device at  $1 \text{ A g}^{-1}$  can be determined to be  $9 \text{ mAh g}^{-1}$ , about  $17\%$  that of the  $\text{Bi}_2\text{O}_3\text{-}6//\text{AC}$  device. The further EIS plot in Figure S10(a) exhibited a tiny arc and a large slope, verifying the relatively small internal resistance and fast mass transfer of the  $\text{Bi}_2\text{O}_3\text{-}6//\text{AC}$  asymmetric device. Based on the previous morphological and structural characterisation, such superior capacitive performance of  $\text{Bi}_2\text{O}_3\text{-}6//\text{AC}$  asymmetric device is derived from the highly crystalline  $\text{Bi}_2\text{O}_3$  nanosheet-assembled porous architecture coupled with many oxygen vacancies.

To assess the possibility of practical application of such water-tailored  $\text{Bi}_2\text{O}_3\text{-}6$  materials, the stability of the  $\text{Bi}_2\text{O}_3\text{-}6//\text{AC}$  asymmetric device was measured. As shown in Figure S10(b), after 2000 cycles of continuous CV testing, an obvious capacity decay was observed, and only  $70\%$  of the initial capacity remained. The CV curves in the inset reflect a change in the contour, directly confirming capacity fading. To further confirm the superior charge-storage performance of the  $\text{Bi}_2\text{O}_3\text{-}6//\text{AC}$  asymmetric device, the energy and power densities were calculated according to Equations (9) and (10) and shown in the Ragone plot (Figure 6f). Specifically, the highest energy density of  $40.8 \text{ Wh kg}^{-1}$  at a power density of  $798 \text{ W kg}^{-1}$  and maintained at  $28.8 \text{ Wh kg}^{-1}$  at a power density of  $7444 \text{ W kg}^{-1}$ . Compared with the previously reported  $\text{Bi}_2\text{O}_3$ -based device, the  $\text{Bi}_2\text{O}_3\text{-}6//\text{AC}$  asymmetric device shows its superiority in terms of charge storage.

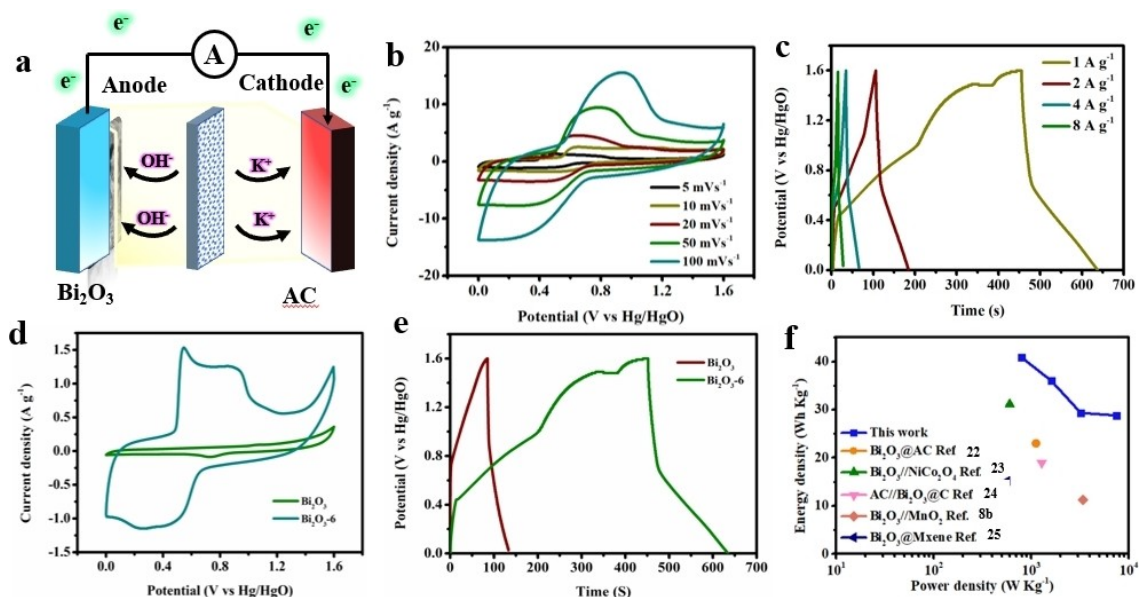


**Figure 6.** a) Construction of  $\text{Bi}_2\text{O}_3$ //AC asymmetric device. b) CV curves of  $\text{Bi}_2\text{O}_3$ -6//AC device from 5 to 100  $\text{mV s}^{-1}$ . c) GCD curves of  $\text{Bi}_2\text{O}_3$ -6//AC device at various current densities. d and e) CV and GCD comparison of  $\text{Bi}_2\text{O}_3$ //AC and  $\text{Bi}_2\text{O}_3$ -6//AC device at 5  $\text{mV s}^{-1}$  and 1  $\text{A g}^{-1}$ . f) Ragone plot of  $\text{Bi}_2\text{O}_3$ //AC device.

## Conclusions

In summary, oxygen-vacancy-enriched  $\text{Bi}_2\text{O}_3$  with a tailored morphology and crystallinity was successfully synthesised by inducing trace water in the solvothermal process. The electrochemical evaluation results confirmed that the capacity and performance of the water-tailored  $\text{Bi}_2\text{O}_3$  were enhanced. The enhanced capacity is mainly derived from the following aspects: i) the tailored tremella-shaped  $\text{Bi}_2\text{O}_3$  with more exposed redox active sites and faster ion diffusion; and ii) the improved crystallinity and created oxygen vacancies to increase the conductivity and promote electron transfer. A remarkable cycle stability is also displayed, with approximately 82% of the initial capacity retained after 1500 cycles of measurement. This study proposes a novel environmental-friendly way to tailor the morphology and create oxygen vacancies in electrode materials with high capacity and stability. In subsequent study, further improving the long-term stability of  $\text{Bi}_2\text{O}_3$  are imperative.

## Experimental Section

### Materials

Bismuth nitrate pentahydrate ( $\text{Bi}(\text{NO}_3)_3 \cdot 5\text{H}_2\text{O}$ , ≥ 99%), acetylene black, active carbon (AC), and polyvinylidene fluoride (PVDF) were obtained from Sinopharm Chemical Reagent Co., Ltd. Ethanol ( $\text{C}_2\text{H}_5\text{OH}$ , 95%), ethylene glycol (EG;  $\text{C}_2\text{H}_6\text{O}_2$ , 98%), N-methyl 2-pyrrolidinone (NMP), and potassium hydroxide (KOH) were purchased from XiLong Scientific. DI water was utilised in all experimental processes (resistance of 18.25 MΩ). All the reagents were used directly without further purification.

### Synthesis of $\text{Bi}_2\text{O}_3$ with various water addition

Typically, 1.96 g of  $\text{Bi}(\text{NO}_3)_3 \cdot 5\text{H}_2\text{O}$  was dissolved in 48 mL of EG to form a transparent solution. 24 mL of ethanol was then poured and stirred until a homogeneous mixture was obtained. Subsequently, the mixture was transferred to a 100 mL Teflon lined-steel autoclave and heated at 160 °C for 5 h. Finally, the  $\text{Bi}_2\text{O}_3$  powder was obtained after washing, filtered and dried for 12 h. Water-tailored  $\text{Bi}_2\text{O}_3$  was obtained by adding a 24 mL ethanol-water mixture as a solvent. Based on the volume of added water, the synthesised  $\text{Bi}_2\text{O}_3$  samples were classified as  $\text{Bi}_2\text{O}_3$ -3,  $\text{Bi}_2\text{O}_3$ -6,  $\text{Bi}_2\text{O}_3$ -12, and  $\text{Bi}_2\text{O}_3$ -24.

### Characterization

The phase structures of various  $\text{Bi}_2\text{O}_3$  were obtained on an X-ray diffractometer (Japan, XRD-6100). The morphology and microstructure were characterised through scanning electron microscopy (SEM, Zeiss) and transmission electron microscopy (TEM, JEOL JEM-F200) coupled with energy-dispersive X-ray spectroscopy (EDS). XPS was performed using an X-ray photoelectron spectrometer (XPS, Thermo Scientific K-alpha). The Nitrogen adsorption-desorption isotherms were obtained using a Micromeritics ASAP 2460 Instruments autosorb iQ equipment at 77.3 K. Electron paramagnetic resonance (EPR) spectra were obtained using a Bruker A300 spectrometer. Mott-Schottky (MS) plots were obtained using an electrochemical workstation (CHI 660E) in 1 M KOH.

### Electrochemical measurement

All the electrochemical tests were performed using an electrochemical workstation (CHI 660E) in 1 M KOH, using platinum foil and Hg/HgO as the counter and reference electrodes, respectively. As reported previously, the work electrodes were prepared by mixing  $\text{Bi}_2\text{O}_3$ , carbon black, and PVDF binder in a weight ratio of 8:1:1 and grinding for an hour in NMP.<sup>[6e]</sup> Subsequently, the slurry-like mixture was evenly spread on a 1 × 1.2 cm<sup>2</sup> nickel foam and dried for 12 h at 60 °C in a vacuum drying oven. The electrochemical performance was evaluated using cyclic voltammetry

(CV), chronopotentiometry (CP), and electrochemical impedance spectroscopy (EIS) measurements. Prior to electrochemical evaluation, 100 CV test cycles were performed to activate the work electrode. EIS tests were performed within a frequency range of  $10^{-2}$ – $10^5$  Hz with a 10 mV amplitude potential. The specific capacity was calculated using the following equations:<sup>[1c]</sup>

$$C_{sp} = I \Delta t / m \Delta V \quad (8)$$

$$E = 1/2 CV^2 \quad (9)$$

$$P = E/3.6\Delta t \quad (10)$$

where,  $C_{sp}$  is the specific capacity ( $\text{F g}^{-1}$ ),  $I$  (A) is the discharge current density,  $\Delta t$  (s) is the discharge time,  $m$  (g) is the weight of the active material, and  $\Delta V$  (V) is the potential window.

## Supporting Information

The authors have cited additional references within the Supporting Information.<sup>[26–29]</sup>

## Acknowledgements

The authors want to convey their appreciation for the National Natural Science Foundation of China (No. 22169008), the Scientific and Technological Project of Education Department (No. 2201351) and the Key Laboratory for Environment and Energy Catalysis of Jiangxi Province (20181BCD40004). This work was also financially supported by the Open Project of Fine Chemical Engineering Technology Research Centre of Jiangxi Province (No. JFCEC-KF-2203) and the Innovation & Entrepreneurship Project of Jiangxi Science and Technology Normal University, P.R. China (No. S202211318066).

## Conflict of Interests

The authors declare no conflict of interest.

## Data Availability Statement

The data that support the findings of this study are available on request from the corresponding author. The data are not publicly available due to privacy or ethical restrictions.

**Keywords:**  $\text{Bi}_2\text{O}_3$  · crystallinity · morphology modulation · oxygen vacancy · trace water

[1] a) J. Mei, T. Liao, G. A. Ayoko, Z. Sun, *ACS Appl. Mater. Interfaces* **2019**, *11*, 28205–28212; b) Y. Zeng, Y. Han, Y. Zhao, Y. Zeng, M. Yu, Y. Liu, H. Tang, Y. Tong, X. Lu, *Adv. Energy Mater.* **2015**, *5*, 1402176; c) Y. Ma, Y. Bai, B. Liang, R. Yang, X. Jiang, S. Zheng, C. Zhang, C. Hu, *Appl. Surf. Sci.* **2022**, *579*, 152156.

- [2] a) X. Xiao, T. Ding, L. Yuan, Y. Shen, Q. Zhong, X. Zhang, Y. Cao, B. Hu, T. Zhai, L. Gong, J. Chen, Y. Tong, J. Zhou, Z. L. Wang, *Adv. Energy Mater.* **2012**, *2*, 1328–1332; b) Y. Zeng, M. Yu, Y. Meng, P. Fang, X. Lu, Y. Tong, *Adv. Energy Mater.* **2016**, *6*, 1601053; c) J. Zhao, Z. Li, X. Yuan, Z. Yang, M. Zhang, A. Meng, Q. Li, *Adv. Energy Mater.* **2018**, *8*, 1702787.
- [3] a) J. Luo, Z. Zheng, A. Kumamoto, W. I. Unah, S. Yan, Y. H. Ikuhara, X. Xiang, X. Zu, W. Zhou, *Chem. Commun.* **2018**, *54*, 794–797; b) Y. Bai, Y. Ma, S. Zheng, C. Zhang, C. Hu, B. Liang, Y. Xu, G. Huang, R. Yang, *Colloids Surf. A* **2002**, *647*, 127896.
- [4] a) J. Xu, Z. Meng, Z. Hao, X. Sun, H. Nan, H. Liu, Y. Wang, W. Shi, H. Tian, X. Hu, *J. Colloid Interface Sci.* **2022**, *609*, 878–889; b) H. G. Tong, S. Chen, J. W. Tu, X. H. Zeng, C. L. Wang, P. C. Wang, Q. W. Chen, *J. Power Sources* **2022**, *549*, 232140; c) S. Yang, L. Qian, Y. Ping, H. Zhang, J. Li, B. Xiong, P. Fang, C. He, *Ceram. Int.* **2021**, *47*, 8290–8299; d) S. Q. Liu, M. R. Gao, R. F. Feng, L. Gong, H. Zeng, J.-L. Luo, *ACS Catal.* **2021**, *11*, 7604–7612; e) S. Q. Liu, E. Shahini, M. R. Gao, L. Gong, P. F. Sui, T. Tang, H. Zeng, J. L. Luo, *ACS Nano* **2021**, *15*, 17757–17768.
- [5] a) J. Zhao, Z. Li, T. Shen, X. Yuan, G. Qiu, Q. Jiang, Y. Lin, G. Song, A. Meng, Q. Li, *J. Mater. Chem. A* **2019**, *7*, 7918–7931; b) R. Liu, L. Ma, G. Niu, X. Li, E. Li, Y. Bai, G. Yuan, *Adv. Funct. Mater.* **2017**, *27*, 1701635.
- [6] a) S. X. Wang, C. J. Jin, W. J. Qian, *J. Alloys Compd.* **2014**, *615*, 12–17; b) D. Qu, L. Wang, D. Zheng, L. Xiao, B. Deng, D. Qu, *J. Power Sources* **2014**, *269*, 129–135; c) D. Yuan, J. Zeng, N. Kristian, Y. Wang, X. Wang, *Electrochim. Commun.* **2009**, *11*, 313–317; d) J. Li, Q. Wu, G. Zan, *Eur. J. Inorg. Chem.* **2015**, *2015*, 5751–5756; e) Y. Ma, Y. Bai, B. Liang, R. Yang, S. Zheng, C. Hu, C. Zhang, F. Qin, L. Wei, *Colloids Surf. A* **2022**, *633*, 127896.
- [7] S. Zheng, Y. Fu, L. Zheng, Z. Zhu, J. Chen, Z. Niu, D. Yang, *J. Mater. Chem. A* **2019**, *7*, 5530–5538.
- [8] a) L. Li, X. Zhang, Z. Zhang, M. Zhang, L. Cong, Y. Pan, S. Lin, *J. Mater. Chem. A* **2016**, *4*, 16635–16644; b) H. Xu, X. Hu, H. Yang, Y. Sun, C. Hu, Y. Huang, *Adv. Energy Mater.* **2015**, *5*, 1401882.
- [9] a) W. Zuo, W. Zhu, D. Zhao, Y. Sun, Y. Li, J. Liu, X. W. Lou, *Energy Environ. Sci.* **2016**, *9*, 2881–2891; b) N. M. Shinde, Q. X. Xia, J. M. Yun, S. Singh, R. S. Mane, K. H. Kim, *Dalton Trans.* **2017**, *46*, 6601–6611.
- [10] a) Z. Deng, T. Liu, T. Chen, J. Jiang, W. Yang, J. Guo, J. Zhao, H. Wang, L. Gao, *ACS Appl. Mater. Interfaces* **2017**, *9*, 12469–12477; b) K. Gopalsamy, Z. Xu, B. Zheng, T. Huang, L. Kou, X. Zhao, C. Gao, *Nanoscale* **2014**, *6*, 8595–8600.
- [11] a) X. Huang, W. Zhang, Y. Tan, J. Wu, Y. Gao, B. Tang, *Ceram. Int.* **2016**, *42*, 2099–2105; b) J. Sun, J. Wang, Z. Li, Z. Yang, S. Yang, *RSC Adv.* **2015**, *5*, 51773–51778; c) Y. Qiu, H. Fan, X. Chang, H. Dang, Q. Luo, Z. Cheng, *Appl. Surf. Sci.* **2018**, *434*, 16–20; d) H. Zheng, H. Li, M. Yu, M. Zhang, Y. Tong, F. Cheng, X. Lu, *J. Mater. Chem. A* **2017**, *5*, 25539–25544; e) T. Qin, X. Zhang, D. Wang, T. Deng, H. Wang, X. Liu, X. Shi, Z. Li, H. Chen, X. Meng, W. Zhang, W. Zheng, *ACS Appl. Mater. Interfaces* **2018**, *11*, 2103–2111.
- [12] a) N. M. Shinde, Q. X. Xia, J. M. Yun, R. S. Mane, K. H. Kim, *ACS Appl. Mater. Interfaces* **2018**, *10*, 11037–11047; b) G. Zan, T. Wu, P. Hu, Y. Zhou, S. Zhao, S. Xu, J. Chen, Y. Cui, Q. Wu, *Energy Storage Mater.* **2020**, *28*, 82–90.
- [13] a) C. Hu, C. Lian, S. Zheng, X. Li, T. Lu, Q. Hu, S. Duo, R. Zhang, Y. Sun, F. Chen, *J. Energy Chem.* **2016**, *25*, 489–494; b) T. Lu, R. Zhang, C. Hu, F. Chen, S. Duo, Q. Hu, *Phys. Chem. Chem. Phys.* **2013**, *15*, 12963–12970; c) C. Hu, T. Lu, F. Chen, R. Zhang, C. Lian, S. Zheng, Q. Hu, S. Duo, *Mater. Res. Bull.* **2014**, *53*, 42–48.
- [14] R. Yi, R. Wang, J. Duan, Z. Fang, H. Li, Z. Chen, A. Zhou, Y. Sun, *Electrochim. Acta* **2020**, *338*, 135845.
- [15] Z. Li, W. Zhang, Y. Tan, J. Hu, S. He, A. Stein, B. Tang, *Electrochim. Acta* **2016**, *214*, 103–109.
- [16] Y. Yan, K. Li, X. Chen, Y. Yang, J. M. Lee, *Small* **2017**, *13*, 1701724.
- [17] H. B. Zheng, Y. X. Zeng, H. Z. Zhang, X. Y. Zhao, M. H. Chen, J. Liu, X. H. Lu, *J. Power Sources* **2019**, *433*, 126684.
- [18] a) S. Li, Y. Cui, R. Kang, B. Zou, D. H. L. Ng, S. A. El-Khodary, X. Liu, J. Qiu, J. Lian, H. Li, *Chem. Commun.* **2021**, *57*, 8182–8185; b) W. Q. Zhu, B. B. Zou, C. H. Zhang, D. H. L. Ng, S. A. El-Khodary, X. H. Liu, G. C. Li, J. X. Qiu, Y. Zhao, S. L. Yang, J. B. Lian, H. M. Li, *Adv. Mater. Interfaces* **2020**, *7*, 2000705.
- [19] X. Wang, W. Wang, J. Zhang, H. Wang, Z. Yang, H. Ning, J. Zhu, Y. Zhang, L. Guan, X. Teng, Q. Zhao, M. Wu, *Chem. Eng. J.* **2021**, *426*, 31867.
- [20] T. T. Qin, X. Y. Zhang, D. Wang, T. Deng, H. X. Wang, X. F. Liu, X. Y. Shi, Z. M. Li, H. Chen, X. M. Meng, W. Zhang, W. T. Zheng, *ACS Appl. Mater. Interfaces* **2019**, *11*, 2103–2111.

- [21] J. Yang, X. Xiao, P. Chen, K. Zhu, K. Cheng, K. Ye, G. Wang, D. Cao, J. Yan, *Nano Energy* **2019**, *58*, 455–465.
- [22] O. Uner, N. Aslan, A. Sarıoğlu, F. Semerci, M. M. Koç, *J. Mater. Sci.* **2021**, *32*, 15981–15994.
- [23] R. H. Yi, R. C. Wang, J. Q. Duan, Fang, Z. Fang, H. S. Li, Z. Y. Chen, A. J. Zhou, Y. M. Sun, *Electrochim. Acta* **2020**, *338*: 135845.
- [24] Z. S. Zhao, Y. H. Ye, W. H. Zhu, L. Xiao, B. H. Deng, J. P. Liu, *Chin. Chem. Lett.* **2018**, *29*, 629–632.
- [25] Q. X. Xia, N. M. Shinde, J. M. Yun, T. F. Zhang, R. S. Mane, S. Mathur, K. H. Kim, *Electrochim. Acta* **2018**, *271*, 351–360.
- [26] L. Gurusamy, S. Anandan, N. Liu, J. J. Wu, *J. Electroanal. Chem.* **2020**, *856*, 113489.
- [27] N. N. Xia, D. S. Yuan, T. X. Zhou, J. X. Chen, S. S. Mo, Y. L. Liu, *Mater. Res. Bull.* **2011**, *46*, 687–691.
- [28] S. T. Senthilkumar, R. K. Selvan, M. Ulaganathan, J. S. Melo, *Electrochim. Acta* **2014**, *115*, 518–524.
- [29] A. Deepi, G. Srikanth, A. S. Nesaraj, *Nano-Struct. Nano-Objects* **2018**, *15*, 10–16.

---

Manuscript received: February 23, 2023

Revised manuscript received: April 23, 2023

Accepted manuscript online: April 27, 2023

Version of record online: May 23, 2023

---